Warm-Air Intrusions in Arizona's Meteor Crater

BIANCA ADLER,* C. DAVID WHITEMAN, SEBASTIAN W. HOCH, AND MANUELA LEHNER

University of Utah, Salt Lake City, Utah

NORBERT KALTHOFF

Institute for Meteorology and Climate Research, Karlsruhe Institute of Technology, Karlsruhe, Germany

(Manuscript received 2 August 2011, in final form 24 January 2012)

ABSTRACT

Episodic nighttime intrusions of warm air, accompanied by strong winds, enter the enclosed near-circular Meteor Crater basin on clear, synoptically undisturbed nights. Data analysis is used to document these events and to determine their spatial and temporal characteristics, their effects on the atmospheric structure inside the crater, and their relationship to larger-scale flows and atmospheric stability. A conceptual model that is based on hydraulic flow theory is offered to explain warm-air-intrusion events at the crater. The intermittent warm-air-intrusion events were closely related to a stable surface layer and a mesoscale (~50 km) drainage flow on the inclined plain outside the crater and to a continuous shallow cold-air inflow that came over the upstream crater rim. Depending on the upstream conditions, the cold-air inflow at the crater rim deepened temporarily and warmer air from above the stable surface layer on the surrounding plain descended into the crater, as part of the flowing layer. The flow descended up to 140 m into the 170-m-deep crater and did not penetrate the approximately 30-m-deep crater-floor inversion. The intruding air, which was up to 5 K warmer than the crater atmosphere, did not extend into the center of the crater, where the nighttime near-isothermal layer in the ambient crater atmosphere remained largely undisturbed. New investigations are suggested to test the hypothesis that the warm-air intrusions are associated with hydraulic jumps.

1. Introduction

Temperature inversions develop regularly in valleys and basins during clear undisturbed nights (Whiteman 2000). In particular, small, completely enclosed basins experience a more enhanced cooling than do valleys because of the absence of the along-valley flows. The nocturnal temperature inversion in a basin often grows until it is approximately equal to the basin depth. If stability inside the basin increases, downslope winds can be suppressed or even a self-shutoff of the downslope flows can occur (Clements et al. 2003). This and a decoupling of the basin atmosphere from the air above combine to produce weak nocturnal winds within a basin stable layer. Such quiescent, stably stratified atmospheres have been reported in various basins in the United States and Europe (e.g., Whiteman et al. 1996; Clements et al. 2003; Steinacker et al. 2007).

Observations in Arizona's Barringer Meteorite Crater (also known as Meteor Crater) during the Meteor Crater Experiment (METCRAX) field campaign of 2006, however, showed different nocturnal temperature profiles and evolution. The typical nighttime evolution of temperature profiles inside Meteor Crater during clear undisturbed nights was analyzed by Whiteman et al. (2008; see their Fig. 10) and is briefly summarized here. A strong 30-m-deep surface inversion forms on the crater floor and is typically surmounted by a deep near-isothermal (i.e., less stable) layer that extends upward to the crater rim. The temperature structure inside the crater is approximately horizontally homogeneous from sidewall to sidewall. The crater atmosphere cools continuously during the night while maintaining the near-isothermal layer structure. Because of the more rapid cooling of the air inside the crater relative to that of the atmosphere above, a capping inversion, which defines the top of the crater

* Current affiliation: Karlsruhe Institute of Technology, Karlsruhe, Germany.

Corresponding author address: Bianca Adler, Institute for Meteorology and Climate Research, Karlsruhe Institute of Technology, POB 3640, 76021 Karlsruhe, Germany.
E-mail: bianca.adler@kit.edu

DOI: 10.1175/JAMC-D-11-0158.1

atmosphere, develops progressively throughout the night; typically at the level of the crater rim. On the slightly sloping plain outside the crater a 30–50-m-deep stable surface layer forms with a near-isothermal layer above, hereinafter called the *residual layer*. A mesoscale southwesterly drainage flow with a flow depth between 100 and 250 m typically forms on the plain (Savage et al. 2008). Observations with a sonic detection and ranging (sodar) device positioned 1.5 km southwest of Meteor Crater from mid-September through mid-October of 2009 showed drainage flows with peak wind speeds of 6–8 m s^{-1} and jet heights of 20–35 m above ground (Hoch et al. 2010). The drainage flow on the plain interacts with the atmosphere inside the crater (Whiteman et al. 2010). Cold air builds up at the rim on the upwind side of the crater. Part of it splits around the crater while a shallow layer of cold air spills over the crater rim and descends partway down the crater's upwind inner sidewall until it reaches its buoyancy equilibrium level. This *cold-air intrusion* was simulated using a mass-flux model (Haiden et al. 2011). This model showed that the detrainment of cold air during its descent into the crater and rising motions inside the crater, which compensate for air descending the sidewalls, destabilize the crater atmosphere and produce the observed near-isothermal lapse rate.

While the shallow inflow of cold air from outside the crater was a common phenomenon that often lasted for most of the night, another unusual phenomenon that affected the temperature structure inside the crater occurred intermittently on some nights. During these discrete events, an elevated warm flow intruded into the crater atmosphere above the upwind sidewall. To our knowledge, this phenomenon, here termed a *warm-air intrusion*, was not previously documented in other enclosed basins.

The aim of this paper is to determine the characteristics of the observed warm-air intrusions into Meteor Crater and to present a conceptual model of the phenomenon. The paper is structured as follows. The topography of Meteor Crater and the meteorological measurements are described in section 2. Section 3 presents observed temperature and wind profiles inside and outside the crater during selected nighttime intensive observational periods (IOPs) and provides analyses of near-surface measurements during IOP nights and for the whole month. Section 4 presents a conceptual model of the phenomenon, and section 5 contains a summary and conclusions.

2. Meteor Crater topography and meteorological data

a. Topography

The near-circular Meteor Crater is located approximately 40 km east of Flagstaff in northern Arizona (Fig. 1a). It was produced by the impact of a meteorite about 49 000 yr ago (Kring 2007). The crater is approximately 170 m in depth and 1.2 km in diameter at the rim. No major saddles or passes break the rim, which extends about 35–50 m above the surrounding uniform plain. The plain slopes gently upward at a mean angle of about 1° toward the Mogollon Rim, a series of elevated mesas 30 km to the southwest of the crater.

b. Meteorological data

Data came from the METCRAX field campaign conducted in Meteor Crater in October of 2006 (Whiteman et al. 2008). Our analyses are focused primarily on IOP nights 1–6 on 7/8, 11/12, 18/19, 20/21, 22/23, and 28/29 October. Observations included synchronous tethersonde ascents from three sites on the crater floor, 3-hourly rawinsondes launched from a site about 5 km north-northwest of the crater (RS-NW in Fig. 1b), seven flux towers, and four lines of surface-based automatic temperature dataloggers.

Rawinsondes launched from the RS-NW site were used to characterize the background meteorological conditions outside the crater. This launch site was located on a small ridge at 1669 m above mean sea level (MSL) [105 m above crater floor (ACF)], that is, about 20–30 m lower than the plain directly surrounding the crater.

Three tethersondes measuring temperature, pressure, humidity, and winds were operated along a west–east line inside the crater (TS-W, TS-C, and TS-E in Fig. 1c). The base elevation of the sounding sites was normally 1564 m MSL (0 m ACF) at TS-C and 1586 m MSL (22 m ACF) at TS-W and TS-E. Some soundings at TS-W were launched farther down the slope at 1571 m MSL (7 m ACF) because of occasional high wind speeds experienced at the original site. Soundings were generally made to about 100 m above the crater rim but were occasionally extended at the center site to about 250 m above the rim. The ascent duration was about 15 min.

Seven heavily instrumented Integrated Surface Flux Facility towers provided near-surface data inside and outside the crater. Five towers were located inside the crater at the west upper (WU; 1604 m MSL and 40 m ACF) and lower (WL; 1573 m MSL and 9 m ACF) sidewalls, the east upper (EU; 1600 m MSL and 36 m ACF) and lower (EL; 1574 m MSL and 10 m ACF) sidewalls, and the crater floor (FLR; 1564 m MSL and 0 m ACF). One tower was placed at the highest point on the crater's west rim (RIM; 1745 m MSL and 181 m ACF), and one was placed on the surrounding plain about 2.5 km southwest of the crater (SW; 1697 m MSL and 133 m ACF). Tower locations are shown in Figs. 1b and 1c. The maximum tower height was either

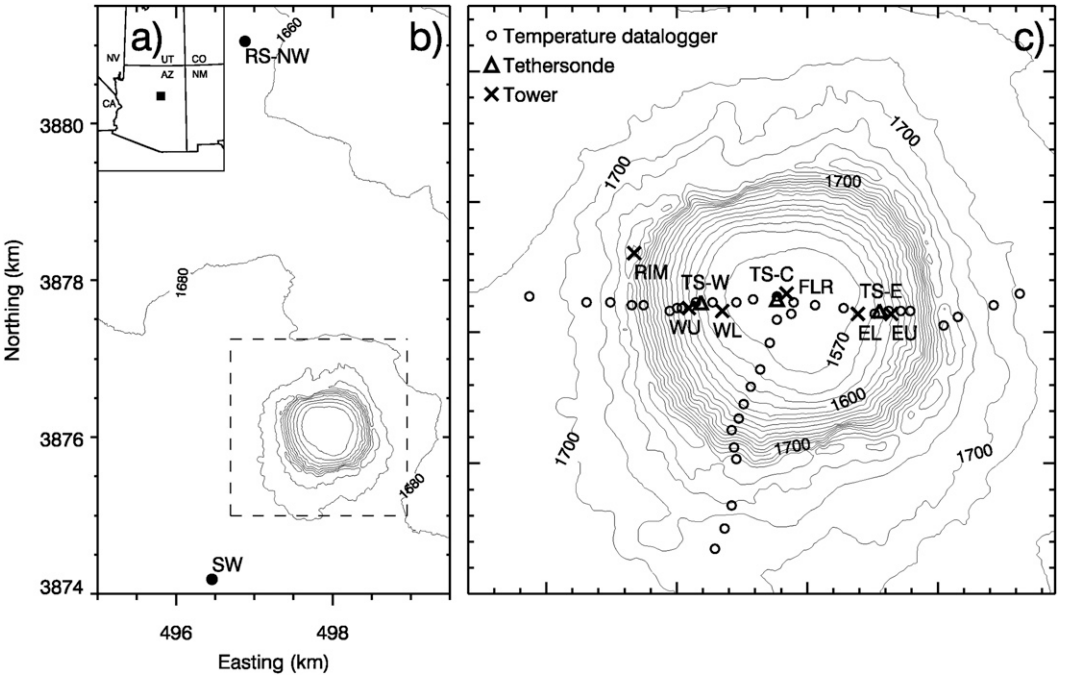

FIG. 1. Universal transverse Mercator zone-12S map of Meteor Crater showing the meteorological instrumentation sites: locations of (a) Meteor Crater in Arizona, (b) the RS-NW and SW sites relative to Meteor Crater, with 20-m altitude contours, and (c) instrumentation in and immediately around Meteor Crater, with 10-m altitude contours. Temperature datalogger lines, indicated by open circles, run up the west, south, and east sidewalls of the crater, extending over the rim and onto the adjacent plain. Tethersondes were flown from sites indicated with triangles on a west–east line through the crater and labeled tethersonde west (TS-W), tethersonde central (TS-C), and tethersonde east (TS-E). Flux towers on the west rim and inside the crater are indicated with an X and are labeled RIM, WU, WL, FLR, EL, and EU.

6 m (WU and EU) or 10 m (SW, RIM, WL, FLR, and EL). Pressure (resolution 0.01 hPa) and temperature data were sampled at 1 Hz, and 3D sonic anemometers sampled the three wind components at 60 Hz, with three-sample averages output at 20 Hz. In a post-processing step, sonic anemometer data were rotated to a surface-parallel, geographic coordinate system using the planar-fit technique (Wilczak et al. 2001). For the rotation, the 5-min-average wind components from the entire project were used. This coordinate system had a project-average slope-perpendicular vertical velocity of zero with a u component defined as positive from west to east and a v component defined as positive from south to north.

Additional data came from three of four lines of temperature dataloggers running from the crater floor center up the west, south, and east sidewalls over the rim and out onto the adjacent plain. Pseudovertical temperature profiles were obtained from these lines at sampling intervals of 5 min. Further information on the field sites, data processing, and additional instrumentation not used in this study is available from Whiteman et al. (2008).

3. Analysis of data

a. Observed temperature and wind fields

1) TEMPERATURE FIELD DURING WARM-AIR-INTRUSION EVENTS

The crater atmosphere underwent changes from the normal structure described in section 1 when the intermittent warm-air-intrusion episodes occurred. For example, Fig. 2a shows the temperature structure at 0000 mountain standard time (MST) on 12 October. To approximate soundings from the plain just outside the crater, a homogeneous atmosphere parallel to the plain surface was assumed and the RS-NW soundings were lifted adiabatically by the 20-m difference in elevation. Temperature and wind profiles at RS-NW, because of this site's location, might differ slightly from the atmospheric profiles on the plain adjacent to the crater. The nighttime temperature structure was mainly as described in section 1 over the plain (RS-NW) and in the center (TS-C) and east-slope (TS-E) profiles, but the west-slope (TS-W) profile showed that warm air was present over the west slope of the crater down to an altitude of about

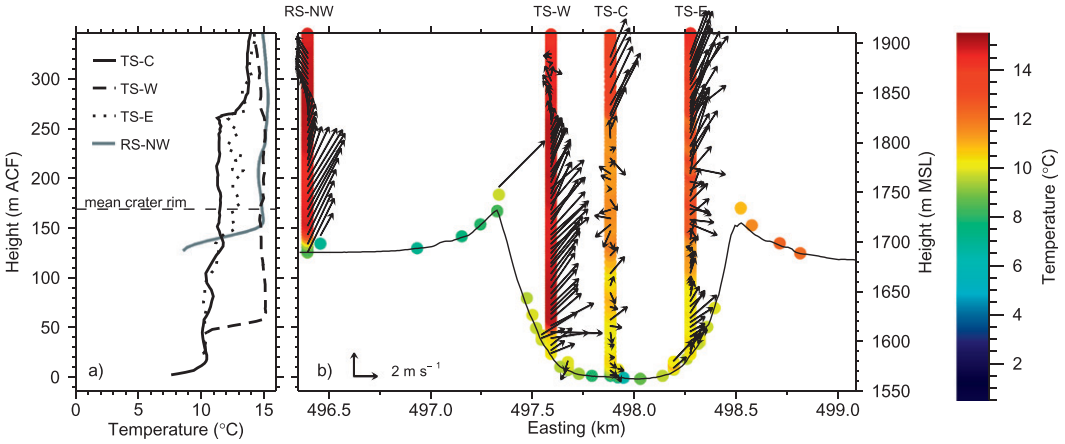

FIG. 2. (a) Temperature profiles from tethersonde soundings from the TS-W, TS-C, and TS-E sites inside Meteor Crater and from a rawinsonde ascent at the RS-NW site outside the crater and (b) west–east cross section through the crater basin with temperature (color coded) and horizontal wind (vectors) measurements from soundings, towers, and temperature dataloggers at 0000 MST 12 Oct. The locations of the measurement sites are projected onto the west–east cross section (black line). The profile RS-NW is not plotted at its real latitude and longitude, and its elevation is adjusted to the topography of the cross section.

49 m ACF. The temperature was about 4°–5°C higher than in the crater center and was similar to that above the plain. The strong capping inversion occurred in the TS-C profile about 100 m above the rim level; that is, the depth of the near-isothermal layer was almost two-thirds higher than usual.

Another warm-air-intrusion event is illustrated in Fig. 3 for 2100 MST 28 October. Here, the warm air over the west sidewall (~3°–4°C warmer than over the crater center) again extended downward into the crater to an elevation of about 49 m ACF. Temperature soundings from all four sounding systems converged into the residual layer above the crater.

There were a significant number of soundings during different IOP nights that showed the characteristics that are so well illustrated in Figs. 2 and 3. Higher temperatures similar to those above the crater extended downward into the crater atmosphere over the west sidewall while profiles over the basin center and east sidewall maintained cooler air and the distinctive near-isothermal temperature structure. In many soundings, as illustrated in Figs. 2 and 3, the temperature profiles at TS-W, while warmer than over the crater center and east sidewall, preserved a near-isothermal stability. In a few cases, the TS-W soundings exhibited higher temperatures and stronger winds at some elevations but not at others, suggesting that the sounding location was at the very edge of the warm-air intrusion or that changes in the temperature structure occurred during the finite time of the tethersonde ascent.

In most cases, the warm air over the west sidewall of the crater did not extend all the way down to the underlying slope and did not affect the cooler near-surface air, as indicated by temperature dataloggers and tower measurements in Figs. 2b and 3b. Near-surface temperature measurements on the plain and on the west outer sidewall and rim showed the typical buildup of cold air on the upwind side of the crater. Its temperature was more than 5°C colder than over the plain to the east of the crater, which was affected by crater outflow. The cold air just upwind of the crater was stably stratified and appeared to form a ''ramp'' for the upper layers of the cold air to flow over the rim into the crater.

Multiple warm-air-intrusion events were observed in tethersonde ascents over the west sidewall on all IOP nights except 20/21 October. Warm-air-intrusion events were seen only in the west-sidewall soundings after 2000 MST; there were no events for which the east-sidewall soundings were significantly warmer than those over the crater center or west sidewall, and there were no events for which the warm-air intrusions over the west sidewall extended to the crater center.

Warm-air intrusions were not always as warm and deep as those illustrated in Figs. 2 and 3, exhibiting variations in both temperature excess and downward extension into the basin. To gain a measure of their strength, we integrated the positive temperature differences between the lowest height of the TS-W soundings and the corresponding heights of the TS-C soundings up to the mean rim height and considered warm-air intrusions to be present over the west sidewall in nighttime soundings (2000–0600 MST) when the integrated temperature difference was greater than 100°C m; that is, for an intrusion depth of 100 m a temperature difference of at least 1°C had to be present

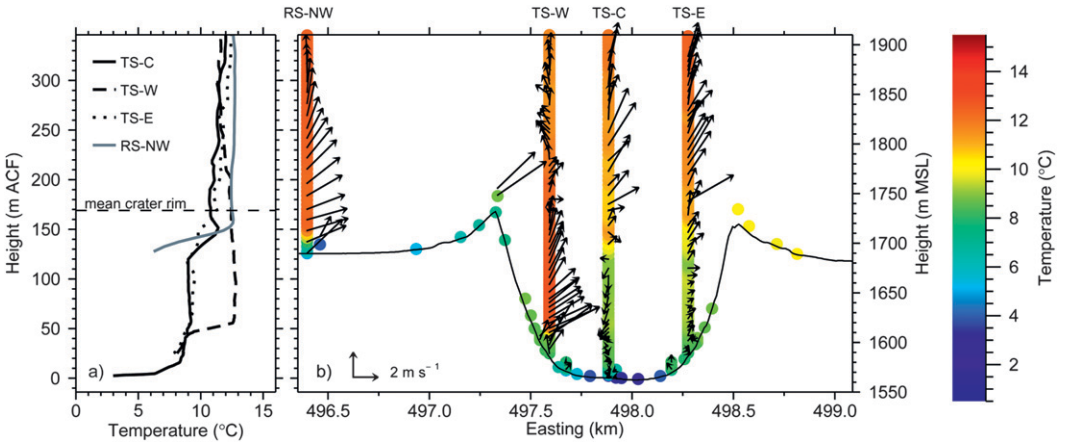

FIG. 3. As in Fig. 2, but for 2100 MST 28 Oct.

at each level. Using this threshold, we detected 16 warm-air-intrusion events out of a total of 70 nocturnal tethersonde ascents; that is, about 23% of all ascents showed warm-air intrusions. The deepest intrusion of warm air (TS-W profile $>$ 1°C warmer than TS-C profile) at the TS-W site ended at approximately 29 m ACF and, thus, extended 140 m into the 170-m-deep crater.

2) WIND FIELD INSIDE AND OUTSIDE METEOR CRATER

During clear undisturbed nights, the RS-NW soundings on the adjacent plain typically exhibited jetlike wind speed profiles, with winds increasing above the surface to speeds of about 5 m s^{-1} at heights at or just above the crater rim and decreasing with further height (Figs. 2b and 3b). The winds were produced by a mesoscale southwesterly drainage flow that developed in the stable atmosphere on the sloping plain that surrounds the crater. Observations and model studies have shown that varying synoptic conditions have a large impact on depth, direction, strength, and evolution of the drainage flow (Savage et al. 2008). The above-described conditions were observed for at least portions of each IOP night except on 20/21 October. Shortly after the drainage flow formed on the respective nights, warm-air intrusions occurred.

Once the crater atmosphere became stable, most profiles within the crater without warm-air intrusions exhibited weak winds with variable directions (not shown), in agreement with results from other enclosed basins (e.g., Clements et al. 2003). During warm-air intrusions, winds remained mainly light and variable in direction in the center and on the east side of the crater atmosphere (Figs. 2b and 3b) while considerably higher wind speeds were observed above the west slope within the warm-air intrusions. The wind speed and direction there were the same as in the mesoscale drainage flow above the surrounding plain. Winds above the crater atmosphere at TS-C and TS-E usually maintained the southwesterly direction characteristic of the mesoscale drainage flow while a stagnant layer occurred above the crater at TS-W.

The synchronicity of the warm-air intrusions and mesoscale drainage flows, their wind direction consistency, and the similar air temperatures between the residual layer at the top of the drainage flow and the air within the warm-air intrusions suggest a close relationship between the two phenomena. Several warm-air intrusions were observed during the night of 11/12 October. On this night a very stable layer was present over the plain with a depth of 40 m above ground relative to the rim relief of 35–50 m (Fig. 4a). A southwesterly drainage flow of about 100-m depth was present, with the maximum wind speed at 60 m above ground (i.e., just above rim level). The upper parts of the drainage flow over the plain developed in the near-isothermal residual layer that was present above the stable surface layer. The winds turned to southeasterly at the top of the drainage flow. During the first half of the night of 28/29 October strong warm-air intrusions occurred. At that time, a 30-m-deep stable surface layer was present over the plain and the mesoscale drainage flow extended into the residual layer to a height of about 150 m above ground (see sounding at 2100 MST in Fig. 4c). Above the drainage flow the wind turned to southerly, producing wind shear. In the second half of this night no warm-air intrusions were measured. During this half of the night, the synoptic conditions changed, the stability of the surface layer on the plain decreased, the drainage flow became more southerly, and its depth decreased to less than 50 m. During the night of 20/21 October, when no warm-air-intrusion events occurred, the stability of the surface layer was weak or nonexistent and a mainly westerly or northwesterly wind increasing with height

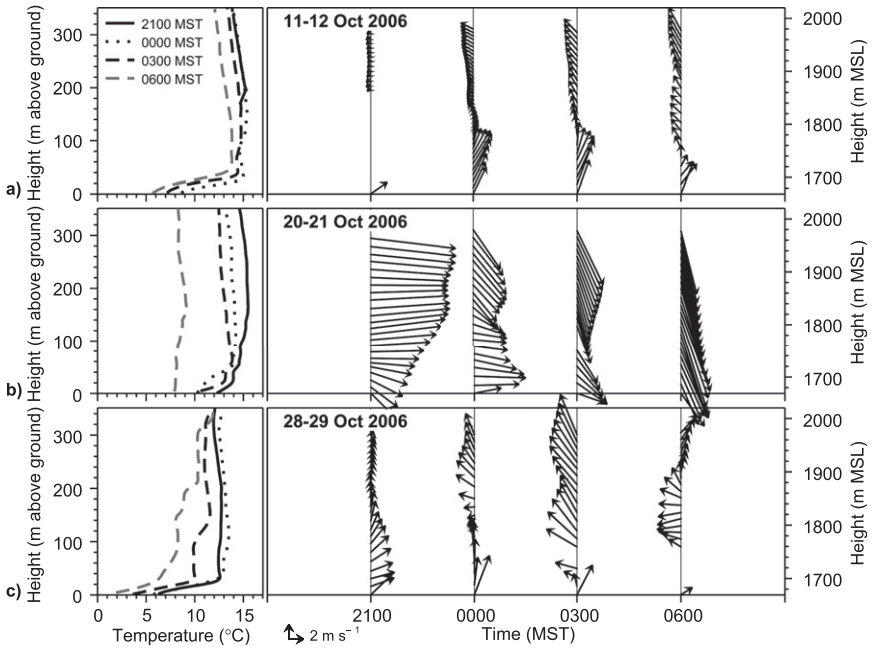

FIG. 4. (left) Temperature and (right) horizontal wind vector profiles from rawinsonde soundings at the RS-NW site outside Meteor Crater on (a) 11/12, (b) 20/21, and (c) 28/29 Oct 2006. Data are missing for the lowest 200 m for the 2100 UTC sounding on 11 Oct and for the lowest 100 m for the 0600 UTC sounding on 29 Oct.

persisted throughout the whole troposphere, with no wind maximum near the surface (Fig. 4b). These observations suggest that the typical preconditions for warm-air-intrusion events were 1) a stable surface layer on the plain with a depth near rim level and with a near-isothermal residual layer above, 2) a southwesterly mesoscale drainage flow 100 m or more in depth, and 3) significant wind shear above the height of the drainage flow jet speed maximum.

b. Origin of the intrusion air

To further understand the warm-air intrusions, we used potential temperature soundings from tethersondes and rawinsondes to determine the origin of the air that entered the crater during warm-air-intrusion events. Potential temperature is a conserved quantity when diabatic processes such as condensation are not present. Air within the warm-air intrusions on the nights of 11/12 and 28/29 October (Fig. 5) had potential temperatures that were nearly identical to those in the residual layer over the surrounding plain. This was typical of most warm-air-intrusion events. Above the crater atmosphere all four soundings (three tethersondes and the rawinsonde) indicated approximately the same potential temperatures. Because the potential temperatures in the warm-air intrusions were very similar to those in the residual layer above the surrounding plain, the intrusion air appeared to originate from this layer and to flow downward into the crater.

Agreement of potential temperatures and similar characteristics of the drainage flow and the wind field at the west side of the crater suggest that they are part of the same flow system (Figs. 2b and 3b). To verify the mass conservation of the flow, we calculated the streamfunction on the plain at RS-NW, TS-W, and TS-C assuming an incompressible, two-dimensional flow and integrated it over the flowing layer, which was characterized by levels with strong westerly wind components. The integrated streamfunctions at RS-NW and TS-W agreed well or were slightly higher at TS-W than at RS-NW. The higher value at TS-W could be caused by sinking motions or by horizontal confluence produced by the three-dimensional crater topography. The integrated streamfunction at TS-C (flowing layer is above the crater atmosphere) was slightly lower than at TS-W, suggesting additional horizontal diffluence and/or turbulent kinetic energy (TKE) production. By applying the continuity equation for an incompressible, two-dimensional flow, we estimated upward motions of up to 2 m s^{-1} in the area with horizontal convergence inside the crater between TS-W and TS-C.

c. Continuous measurements

The infrequent and limited numbers of tethersonde soundings allowed only a rough estimate of the duration,

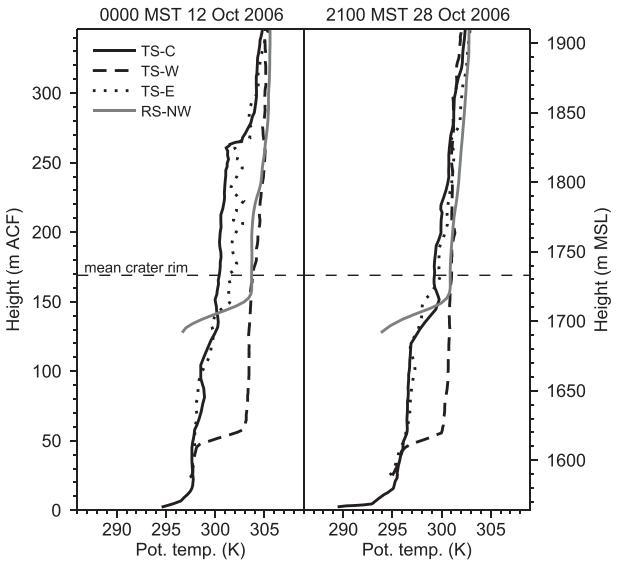

FIG. 5. Potential temperature profiles from tethersonde soundings at TS-W, TS-C, and TS-E inside and from rawinsonde soundings at RS-NW outside Meteor Crater.

frequency, and strength of warm-air-intrusion events. Therefore, we tried to find proxy indicators for warm-air intrusions using the continuous near-surface meteorological measurements in the crater.

1) PRESSURE DIFFERENCE

Because the density of warm air is lower than that of cold air, we assumed that a proxy signal for warm-air intrusions would be found in the difference in surface pressures between the west sidewall flux towers WU and WL, which were below the warm-air intrusion, and the flux towers on the crater floor (FLR) and on the crater's east sidewall (EU and EL), which were not below the warm-air intrusion.

Examples of the 1-min-average pressure differences between the site pairs are shown for IOP nights on 11/12 and 28/29 October in Figs. 6a–c and 7a–c, respectively. For easier comparison we plotted oscillations around zero by subtracting the respective nightly mean (1900–0600 MST) from the pressure differences. Pressures are expected to be lower under the warm-air intrusions, so that differences between the west-sidewall sites and the floor or east-sidewall sites would be negative during warm-air-intrusion events.

The WU–FLR pressure differences exhibited strong fluctuations of maximum amplitude 0.2 hPa while simultaneously the EU–FLR pressure differences were weak (amplitudes below 0.05 hPa) during most IOP nights. Only on 20/21 October, the night without warm-air intrusions, did the EU–FLR pressure-difference oscillations have the same strength as at WU–FLR (not shown). The EU–FLR pressure differences exhibited a weak continuous decrease during most IOP nights. This trend was also apparent at WU–FLR, although it was often disturbed by larger variations during the night. In looking at all October nights, we found that under undisturbed clear-weather conditions the EU–FLR pressure difference typically decreased during the night with an amplitude of about 0.1 hPa. This was produced by colder nighttime air over the basin center than over the sidewalls. The air adjacent to the crater floor was colder by night and warmer by day than the air over the sidewalls. Because WU and EU were about 40 m higher than FLR, this contributed to a nighttime decrease of the WU–FLR and EU–FLR pressure differences. The smaller height differences between the towers on the lower sidewalls at WL and EL and FLR (~10 m) explained why hardly any continuous decrease during the night was visible for these site pairs (Figs. 6b and 7b). Analysis of the WU–FLR and EU–FLR pressure differences indicated that the strong fluctuations in the WU–EU pressure differences in Figs. 5c and 6c were caused primarily by pressure decreases at WU.

The duration and frequency of negative pressure differences varied for the different nights. On 11/12 October, WU–FLR and WU–EU pressure difference oscillations were distinct, with many strong negative-pressure-difference events, some lasting for almost an hour (Figs. 6a and 6c). In contrast, on 28/29 October one main period of strong WU–FLR and WU–EU negative pressure differences occurred in the first half of the night between about 2000 and 2230 MST with only short interruptions (Figs. 7a and 7c). Two additional periods of strong negative pressure differences were observed in the second half of the night, both of them shorter than 15 min. Soundings with strong warm-air intrusions (i.e., high temperature differences and deep penetrations) were correlated with strong negative WU–FLR and WU–EU pressure differences. To estimate the influence of the warm air over the west sidewall on the surface pressure, we calculated the pressure difference at the bottom of two air columns with the same depth and the same pressure at their top but with different temperatures. Under typical ambient conditions at the crater, the hydrostatic pressure difference at the bottom of two columns of 100-m depth with a temperature difference of 3°C was about 0.11 hPa. Similar temperature differences and intrusion depths occurred frequently during warm-air-intrusion events, and the resulting pressure difference near the surface agreed well with the scale of the observed oscillation in the pressure difference WU–EU. Thus, there is strong evidence that warm-air intrusions caused the pressure decreases at WU.

There are many meteorological events that are known to affect pressures in basins, and therefore, for a more complete analysis, we briefly discuss other hydrostatic and

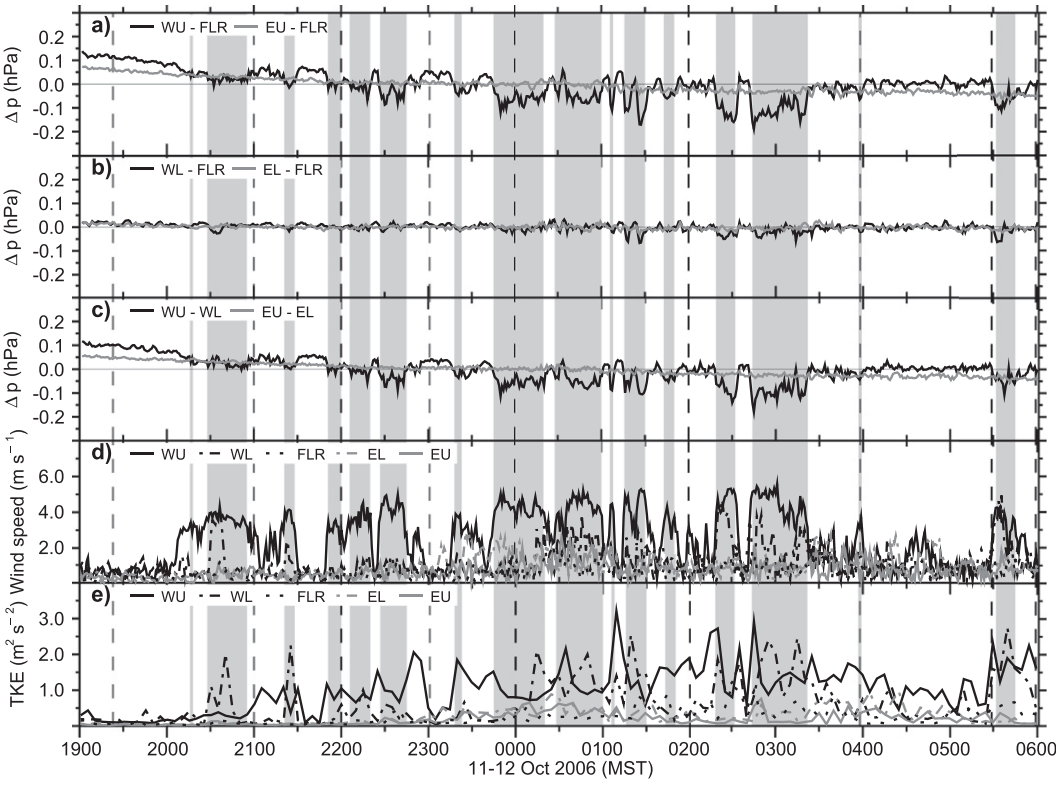

FIG. 6. Time series of the 1-min-average (a) pressure difference Δp between WU and FLR and between EU and FLR, (b) Δp between WL and FLR and between EL and FLR, (c) Δp between WU and WL and between EU and EL, and (d) terrain-following wind speed and (e) 5-min-average TKE at 5 m above ground on 11/12 Oct. The gray dashed vertical lines mark the launch times of tethersonde soundings, the black dashed vertical lines indicate soundings with warm-air intrusions (consider the ~15-min tethersonde ascent time), and the gray-shaded areas indicate times with warm-air intrusions as determined from pressure and wind measurements.

dynamic processes that might affect pressure differences between the different towers. Synoptic-scale influences were largely excluded from consideration by the small horizontal scale of the pressure differences, since tower separations were small (e.g., approximately 380 m for WU and FLR and approximately 770 m for WU and EU).

As mentioned above, the evolution of the cold-air pool inside the crater had a hydrostatic impact on the pressure inside the crater and caused a continuous decrease of the pressure difference between the upper towers and FLR during the night. Because the cold-air pool was horizontally homogeneous, however, it likewise affected the WU–FLR and EU–FLR pressure differences.

As described in section 1, cold air spilled over the crater rim on the upwind side of the crater and descended partway down the crater's inner sidewall (Whiteman et al. 2010). Pseudovertical temperature profiles from temperature datalogger lines at the west and east sidewalls of Meteor Crater typically showed cooler temperatures on the west sidewall (Fig. 8a). The onset of the cold-air intrusions was typically between 1900 and 2000 MST (i.e., shortly after the mesoscale drainage flow developed on the plain), and they occurred more or less continuously throughout the night (Fig. 8b). Cross-basin temperature differences were largest at the crater rim and decreased with decreasing elevation inside the crater. The colder air near the west sidewall contributed to a higher hydrostatic pressure at the west sidewall and, thus, to higher WU–FLR and WU–EU pressure differences. Therefore, it could not explain the intermittent very low pressure at WU.

Gravity waves are ubiquitous in stable boundary layers (e.g., Viana et al. 2007). At the crater, gravity waves generated in the stable boundary layer over the surrounding plain or produced by airflow over the crater rim (Fritts et al. 2010) could affect the pressure difference inside the crater as they crossed the crater, depending on their wavelength. To detect gravity waves on the plain, we applied a trend-removal technique to the surface pressure measured at SW. The resulting pressure oscillations had a maximum amplitude of ~0.05 hPa, which is in accordance with values found for typical pressure fluctuations

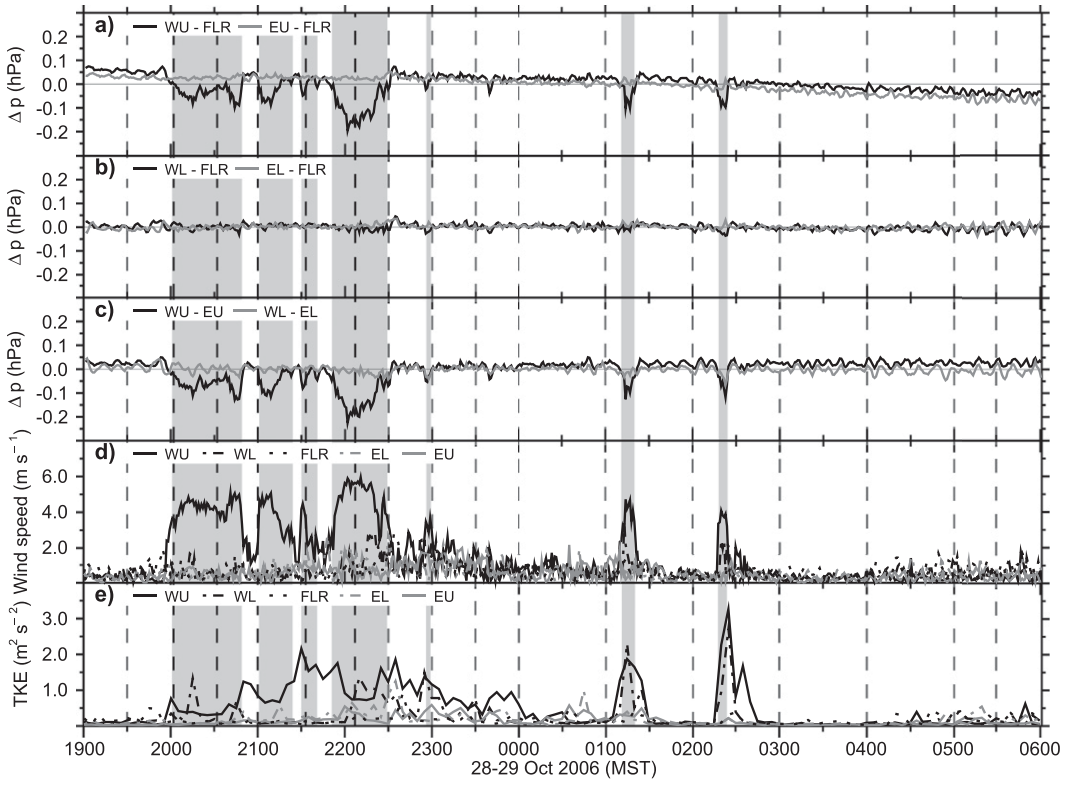

FIG. 7. As in Fig. 6, but on 28/29 Oct.

related to internal waves in the nocturnal stable boundary layer on a plain (Nappo 2002; Viana et al. 2007). These gravity waves, even if they propagated over the crater with a wavelength that produced pressure differences between the sidewall towers, could not explain the high amplitude of pressure fluctuations at WU.

Seiches and gravity waves of various frequencies and amplitudes could also develop internally within the stable atmosphere of the crater. Because of the small amplitudes of the resulting pressure oscillations, the periodic character of the waves, and the symmetric topography of the crater basin, however, these could not produce the strong pressure fluctuations seen only at WU, but would be present at all sites. The cross-basin pressure differences thus appear to be a signature of warm-air intrusions over the west sidewall, because they have the ability to generate pressure differences of the observed amplitude and length scale.

Fluctuations in the WL–FLR pressure difference were significantly damped relative to the WU–FLR fluctuations (Figs. 6a,b and 7a,b). This means that warm-air intrusions generally did not extend to the atmosphere above the WL tower. This is remarkable considering that the horizontal distance between WU and WL was only about 130 m. The warm-air intrusions were thus very strongly confined to an elevated region of the crater atmosphere in the immediate lee of the upwind crater rim, and they extended less than 400 m out into the crater basin.

2) WIND SPEED AND TKE INSIDE THE CRATER

Another indicator of warm-air intrusions was found in wind speed measurements at the flux towers inside the crater. One-minute-average wind speed and 5-min-average turbulent kinetic energy at 5 m above ground are shown in Figs. 6d and 6e, respectively, for 11/12 October and in Figs. 7d and 7e, respectively, for 28/29 October. The TKE per unit mass was calculated as

$$\mathrm{TKE} = 0.5(\overline{u'^2} + \overline{v'^2} + \overline{w'^2}),$$

where u', v', and w' describe the turbulent parts of the wind field. Note that the general features of the wind and turbulence evolution that are discussed below were found at all heights down to 0.5 m above ground, although they were less pronounced at the lower heights.

During the night, wind speeds at FLR, EL, and EU were generally low (<1 m s^{-1}), as expected in a basin atmosphere under stable conditions (see section 1). Wind speeds increased at all towers only when large-scale disturbances mixed out the air in the crater and

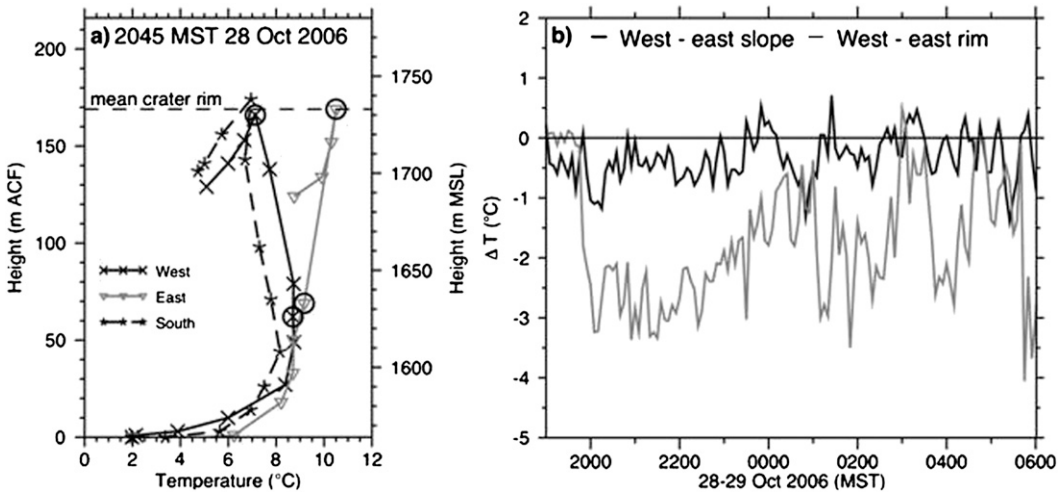

FIG. 8. (a) Pseudovertical temperature profiles from three lines of temperature dataloggers running up the west, east, and south inner sidewalls of the crater to the rim level and out onto the adjacent plain, and (b) temperature difference ΔT between the west and east sidewall (black line) and between the west and east rim (gray line) on 28/29 Oct. The black circles in (a) indicate the dataloggers for which time series are plotted in (b).

coupled the crater atmosphere to the atmosphere above (not shown). However, there were occasional nocturnal periods during which wind speeds at WU (and sometimes at WL) increased up to 6 m s^{-1} while wind speeds remained low at the crater floor and east sidewall (Figs. 6d and 7d). These events were highly correlated with WU–FLR and WU–EU negative pressure differences. For example, the mean correlation for the WU wind speed at 5-m height and the WU–EU pressure differences between 2000 and 0600 MST was −0.90 for IOP nights with warm-air intrusions. On 20/21 October, an IOP night with no warm-air intrusions, the correlation coefficient was −0.07.

Similar to wind speed, TKE increased at WU (and also sometimes at WL) during periods with negative pressure differences (Figs. 6e and 7e). This was very clear on 28/29 October with values at WU exceeding 3 m^2 s^{-2} during negative-pressure-difference periods and being close to zero during the rest of the night. During the night of 11/12 October, TKE inside the crater was generally higher and the correlation with negative pressure differences was less pronounced. The mean correlation coefficient for 5-min-averages of TKE at WU and WU–EU pressure differences on IOP nights with warm-air intrusions was −0.32. We conclude that the high wind speed and TKE at WU were related to the warm-air-intrusion events and not to the cold-air intrusions investigated by Whiteman et al. (2010) and use them as an additional proxy for warm-air intrusions.

Because of the above-described results, near-surface measurements of pressure and wind speed appear to be useful proxies for detecting warm-air intrusions. We accordingly defined the following criteria to identify warm-air-intrusion periods. 1) The WU–EU pressure difference minus the nightly mean was negative. We did not use a numerical threshold for the pressure difference because subtracting the nightly mean often damped the negative amplitude of the oscillations and some warm-air-intrusion periods would have been missed. 2) Wind speeds at the 5-m level at WU exceeded 2 m s^{-1} and wind speeds at the 5-m level at FLR, EL, and EU were less than one-half of the wind speed at WU. We did not use a constant value of wind speed at FLR, EL, and EU for the second criterion because this allowed us to consider nights on which background wind speeds in the crater were slightly higher than normal. When strong momentary fluctuations in the pressure difference and wind speeds occurred, we considered periods that fulfilled the two criteria as a single warm-air-intrusion period when gaps were less than 5 min. In addition, the periods had to last at least 3 min. Periods of warm-air intrusions as detected with this method are marked with the gray shading in Figs. 6, 7, and 9.

3) TEMPERATURE AND WIND SPEED AT THE CRATER RIM

Temperature and wind speed observations at the highest point of the west rim at the RIM tower (12 m higher than the mean rim height of 169 m ACF) were another strong indicator of warm-air-intrusion events (Fig. 9). Strong fluctuations in RIM temperature and wind speed on a time scale of a few minutes occurred. The onset of warm-air intrusions was usually associated with a temperature decrease (maximum decrease of

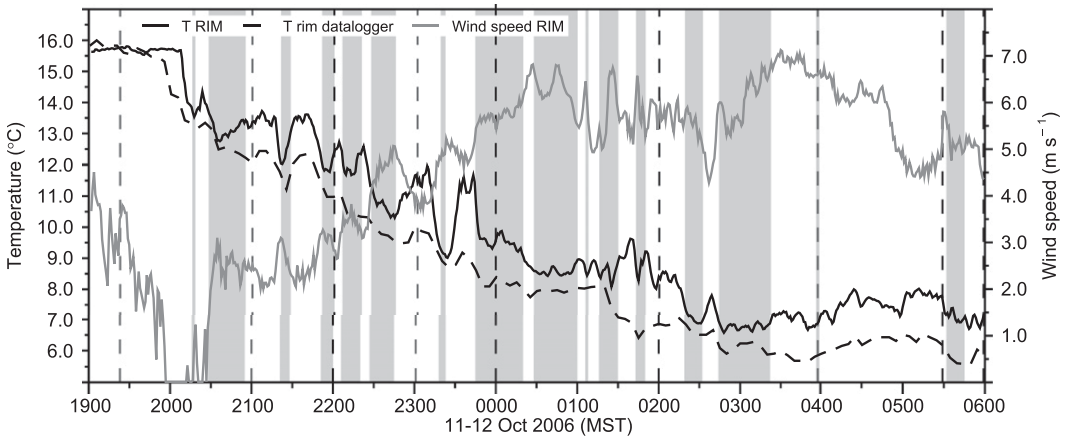

FIG. 9. Time series of 1-min-average 2-m temperature and 10-m wind speed at RIM (181 m ACF) and of 5-min-average temperature from the temperature datalogger on the west crater rim (166 m ACF) on 11/12 Oct. Shaded areas indicate times with warm-air intrusions as determined from pressure and wind measurements.

~3°C) and a wind speed increase (maximum increase of ~2 m s^{-1}) at RIM, and their cessation was normally combined with a temperature increase and a wind speed decrease. The temperature at the lower elevation of the west crater rim (166 m ACF) remained approximately the same, which indicates that during warm-air intrusions a deeper layer of cold air flowed over the crater rim.

Two possible processes may explain the temperature decrease at RIM associated with the initiation of warm-air-intrusion events. First, the events could be driven by pulses of deeper inflows over the rim that are produced by cold-air avalanches off the flat-topped mesas on the Mogollon Rim that are then advected down the mesoscale slope to the crater. Second, temporary enhancement of cold-air transport over the rim could occur as the colder, low-level flow on the plain that is normally mainly diverted around the crater ascends the upwind slope of the crater and flows over the rim. Such events could be driven by oscillations in the strength or stratification of the approaching mesoscale drainage flow. This can be illustrated in terms of the Froude number Fr $[=U/(NH)]$, where U is the approach flow speed, N is the Brunt–Väisälä frequency, and $H = 50$ m is the rim height. If Fr < 1, a dividing streamline separates the lower part of the approaching flow that splits around the crater from the upper part that goes over the rim. Under typical upwind conditions during the onset of warm-air intrusions ($N = 0.09$ s^{-1} and $U = 3$ m s^{-1}), the height of the dividing streamline was $H_{ds} = H(1 - \mathrm{Fr}) \approx 16.7$ m. The air at RIM could thus originate from about 33 m below the rim, resulting in a temperature decrease of some degrees as shown in Fig. 9. The wind speed increase at RIM can either reflect changes in the upstream flow or result from strong leeside winds (cf. Fig. 6 in Durran 1986). The time resolution of our data is insufficient to determine whether the wind speed increase at RIM precedes or follows the initiation of the warm-air intrusion, however.

d. Statistics of warm-air intrusions

Because near-surface pressure and wind speed data were available for all of October in 2006, they could form the basis for a statistical study of the warm-air intrusions, which were mainly identified with the criteria described in 3c(2). Similar to the IOP nights with observed warm-air intrusions, several non-IOP nights showed a very high correlation between WU–FLR pressure differences and wind speed at WU. On the other hand, other non-IOP nights exhibited no correlation at all, similar to 20/21 October, when no warm-air intrusions occurred.

The number of warm-air intrusions and their total and mean duration for every night of October are displayed in Fig. 10. We identified 138 periods of warm-air intrusions on 17 nights, with a mean duration of about 13 min. The first six nights of October had no warm-air intrusions. From 7 to 23 October warm-air intrusions were detected every night except 9/10, 16/17, and 20/21 October. No intrusions occurred on the nights of 24/25 and 25/26 October, followed by the final three nights of warm-air intrusions. A brief description of the overall synoptic conditions in the vicinity of Meteor Crater can be found in the Whiteman et al. (2008) METCRAX overview paper. We found no obvious relationship between warm-air intrusions and general synoptic conditions except that the warm-air intrusions did not occur when the atmosphere was well mixed by synoptic disturbances, which inhibited the formation of mesoscale drainage flows on the plain.

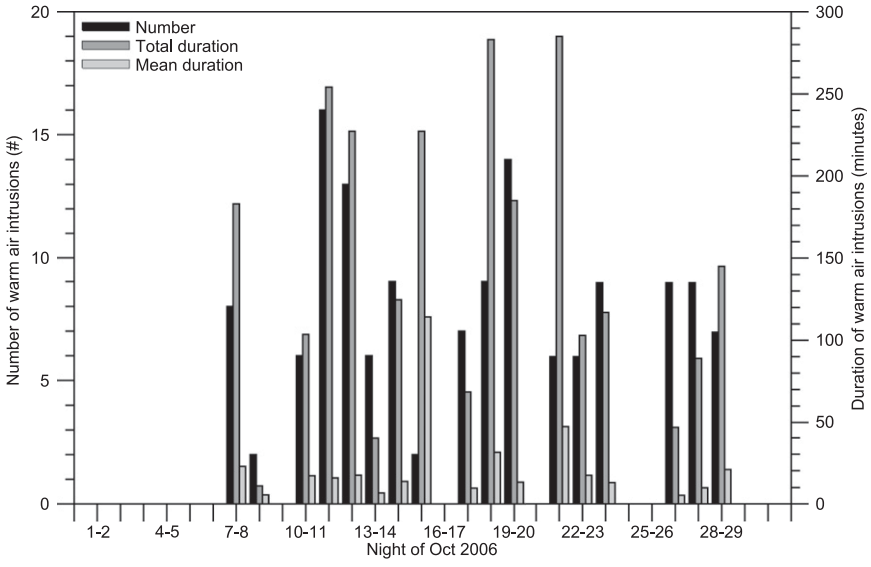

FIG. 10. Total number, total duration, and mean duration of warm-air intrusions for all nights (2000–0600 MST) of October 2006.

The nighttime wind direction at the 10-m height at SW was predominantly from the southwest for the October nights showing the influence of the drainage flows. We did not have temperature and wind data above 10 m AGL on the plain during non-IOP nights because rawinsonde soundings were made only during IOP nights and because continuous vertical profiles of horizontal winds from a radar wind profiler at the same site did not resolve winds below 140 m above ground. Further, a minisodar located at SW did not function properly after lightning struck nearby in early October. Thus, no information about flow depth and level of wind speed maximum could be obtained during non-IOP nights.

e. Characteristics of warm-air intrusions

The previous data analysis provides information about the general characteristics and necessary preconditions for the warm-air intrusions, as follows.

1) Warm-air intrusions occurred episodically on about 50% of all nights, lasting from several minutes to hours, but never through the whole night. The mean duration was 13 min.
2) Warm-air intrusions occurred only on nights during which a stable surface layer was present on the plain outside the crater with a depth near the height of the rim and with a stable residual layer above, when a mesoscale southwesterly drainage flow evolved on the plain and extended into the residual layer, and when wind shear occurred above the height of the drainage-flow-jet speed maximum.
3) The onset of warm-air intrusions was associated with a decrease in temperature and an increase in wind speed at the RIM site. This indicates that a deeper layer of cold air flowed over the crater rim during warm-air-intrusion events.
4) Warm-air intrusions always formed in the immediate lee of the upwind rim as a solitary phenomenon and generally extended less than 400 m out into the crater basin. Their vertical penetration depth into the crater was up to 140 m, and they never penetrated the crater floor inversion. Strong upward motions occurred at the trailing edge of the warm-air intrusion.
5) The flow within the warm-air intrusion had about the same wind speed and wind direction as the mesoscale drainage flow on the plain. Similar wind speeds and directions occurred above the center and eastern crater atmosphere while a stagnant layer existed at the same levels above the western part of the crater.
6) The drainage flow outside the crater, the flow within the warm-air intrusions above the inner west slope, and the flow above the crater atmosphere over the center and eastern slope were part of the same flow system, and mass was conserved.
7) The warm-air originated from the residual layer over the plain.
8) During warm-air intrusions, high values of wind speed and TKE were measured at all levels of the upper west slope tower, whereas wind speed and turbulence remained weak in the ambient atmosphere over the basin center and the east sidewall during the events.

9) During some warm-air intrusions, the depth of the near-isothermal layer over the crater center increased by almost two-thirds of its normal depth.
10) No development of the warm-air-intrusion depth was observed; that is, we did not have any observations in which the warm-air intrusion progressed slowly down the slope. A growth of the intrusion into the crater atmosphere could exist and not be captured with the available observations, however.

4. Conceptual model

On the basis of the warm-air-intrusion characteristics (section 3e), we believe that their occurrence was controlled by the conditions in the stratified flow approaching the crater rim. To explain the observations, we considered several phenomena that are known to occur in stratified flows over obstacles (Smith 2003), including lee waves, Kelvin–Helmholtz instabilities, wakes, wave breaking, and hydraulic jumps. These flows are extremely complex, and the individual flow-regime occurrences depend on upstream profiles of stability and horizontal wind speeds and obstacle characteristics, including height and width.

Lee waves, Kelvin–Helmholtz instability, and wakes do not match the observed warm-air-intrusion characteristics. However, the observed temperature and wind fields in the Meteor Crater during warm-air-intrusion events do have similarities to prior analyses of downslope windstorms [e.g., the intense 11 January 1972 windstorm in Boulder, Colorado, described by Lilly (1978)], although the Meteor Crater events occurred on a much smaller scale. In previous studies, the importance of upstream stability and vertical wind shear and the existence of critical layers for the evolution of strong lee winds are emphasized (e.g., Jiang and Smith 2003). A change in atmospheric stability and/or reduced cross-barrier wind components can form a critical layer, which can either reflect vertically propagating mountain waves resulting in a low-level amplification (Peltier and Clark 1979) or decouple the low-level flow, which allows it to behave hydraulically (Smith 1985; Baines 1995). The hydraulic shallow flow is often decoupled from a stagnant well mixed air layer aloft by a streamline, which is referred to as a critical streamline (Smith 1985; Smith and Sun 1987).

Strong lee winds are often explained by applying the hydraulic-flow theory of stratified fluids over obstacles to the atmosphere (Long 1954; Durran 2003). If the flow regime upstream of a ridge is subcritical (i.e., the fluid thins and accelerates approaching the ridge) and if the acceleration is sufficient, the flow can undergo a transition from subcritical to supercritical at the ridgetop. The supercritical flow accelerates as it descends, producing very high wind speeds down to the bottom of the lee slope. The flow eventually recovers to ambient downstream conditions in a hydraulic jump. Downwind of the hydraulic jump the flow speed is weaker and the flowing-layer depth is higher. Some limitations arise when applying the hydraulic-flow theory to the dynamics of downslope winds in the atmosphere because the atmosphere is an unbounded continuously stratified fluid (Durran 2003). The conditions at Meteor Crater differ from most previous studies on strong lee winds because of the stable atmosphere in the lee of the ridge. Foehn windstorms, another case of strong lee winds, usually do not penetrate into the stable atmosphere of valleys (Mayr and Armi 2008) or do not develop with stable downstream conditions (Mayr and Armi 2010). A destabilization of the valley atmosphere is necessary for the air to descend to the valley floor. At Meteor Crater the continuous cold-air intrusion provides a destabilization mechanism for the air inside the crater (Whiteman et al. 2010; Haiden et al. 2011).

Considering the parallels between the warm-air-intrusion events and downslope windstorms, we offer the following conceptual model (Fig. 11) as a likely explanation of the warm-air-intrusion events at Meteor Crater: During clear undisturbed nights, a very stable surface layer with a lower stability in the residual layer aloft forms outside the crater. On the sloping plain, a mesoscale drainage flow develops that extends above the stable surface layer and the rim. The height of the jet wind maximum and the depth of the stable surface layer are similar to the rim height. A shallow cold-air layer flows continuously over the upwind rim down the inner sidewall and destabilizes the crater atmosphere. The relative depths of the stable surface layer, the drainage flow, and the rim relief are such that small changes in the upwind conditions can suddenly change the flow regime. Shallow cold-air intrusions and a splitting of much of the flow around the crater can suddenly change to a deepening of the cold-air layer flowing over the rim either because of an increase in approach-flow speed or cold-air avalanches (not illustrated in Fig. 11). This causes the flow to undergo a transition from subcritical to supercritical at the rim crest. The inner crater sidewalls are long and steep enough to allow for sufficient supercritical flow acceleration and the potential development of a hydraulic jump. Cold and warm air, both part of the flowing layer, penetrate the crater atmosphere following the underlying topography of the inner upstream sidewall, forming a wavelike flow structure with strong upward motions at its trailing edge. Vertical overshooting above the crater center indicates the nonhydrostatic behavior of the

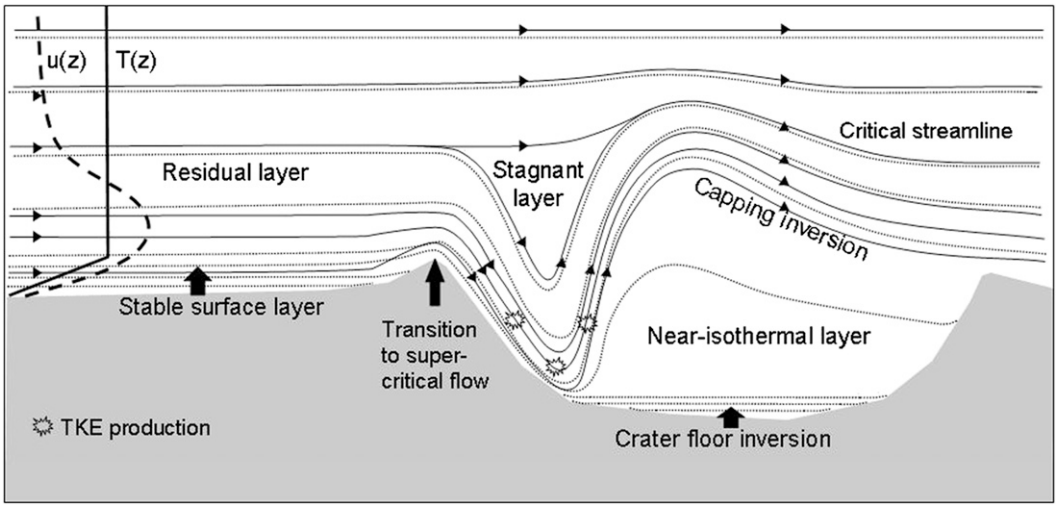

FIG. 11. Conceptual model for warm-air intrusions. Isentropes of potential temperature (dotted contours) and streamlines (solid contours) are indicated. A stratified flow with a stable surface layer and a residual layer above approaches the crater rim. When the cold-air layer flowing over the rim deepens, the flowing layer (levels with high wind speed perpendicular to the rim) undergoes a transition from subcritical to supercritical at the rim crest and penetrates the crater, forming a wavelike flow structure. The capping inversion on top of the crater atmosphere rises above the crater center, indicating a vertical overshooting. A stagnant layer forms above the flowing layer encompassed by a critical streamline. In areas with strong wind shear, TKE is produced.

phenomenon. Durran 1986 identified flows with a nonhydrostatic response that had a similar dimensionless number Na/U as the flow at Meteor Crater, where a is the half-width of the crater slope. Above the crater rim the critical streamline divides and encompasses a stagnant layer above the flowing layer. The ambient crater atmosphere in the center and east remains mainly unaffected, and the approximately 30-m-deep crater floor inversion keeps the flow from penetrating all the way to the crater floor. In areas with strong wind shear, TKE production occurs.

Because the warm-air intrusions were controlled by the drainage flow, we expect them to be strongest in the lee of the rim on the upwind side of the crater. The drainage flow often had a relatively strong southerly component (indicated by the strong cold-air intrusion on the south sidewall in Fig. 8a), and it is very likely that warm-air intrusions into the southwestern and southern parts of the crater occur even more often than observed from wind and pressure data on the west sidewall and from the west sidewall tethersonde soundings.

The conceptual model (Fig. 11) shows similarities to and differences from classical hydraulic jumps for two-layer fluids. The similarities include 1) an initial supercritical, accelerating, and descending flow producing strong winds near the surface in the lee of the rim; 2) a descent of potentially warmer air from aloft; and 3) ascending streamlines. In contrast with the classical hydraulic jump, however, the flow penetrates a stably stratified basin atmosphere, which remains largely undisturbed, and a flowing layer exists above the stable basin atmosphere. Two possible explanations for the latter follow: First, the energy of the flow may not be fully dissipated in the jump and mixing of momentum may be limited by reduced turbulence, with the result that a flowing upper layer remains. Second, the intruding potentially warmer air separates from the underlying cold air and forms a standing singular lee wave, with no hydraulic jump. To investigate further the nature of the warm-air intrusions and to test our conceptual model, additional measurements and/or numerical model studies are necessary.

5. Summary and conclusions

Data analysis from the METCRAX field campaign in Arizona's Meteor Crater provides evidence for warm-air-intrusion events inside the crater basin. The unique topography of Meteor Crater, a symmetric 170-m-deep basin with a uniform rim extending only about 35–50 m above a slightly sloping plain, allowed their development. The events occurred episodically on more than 50% of all nights of the month-long campaign. We hypothesize that oscillations of upstream conditions on the plain outside the crater changed the flow regime so that a deeper layer of cold air flowed over the rim crest, underwent a transition from subcritical to supercritical flow at the crest, followed the topography of the upwind

inner crater sidewall, and accelerated. The upper part of the flowing layer that penetrated into the crater in the immediate lee of the upwind rim was warmer than the air in the crater basin and, thus, formed a warm-air intrusion. Once the flow reached the stronger stability in the lower altitudes of the crater, the streamlines rebounded, rising rapidly above the crater, and leaving the atmosphere over the crater center and east slope undisturbed. A conceptual model of this flow behavior is presented as Fig. 11.

Further studies are needed to verify our hypothesis that the warm-air intrusions are associated with hydraulic jumps. The dataset used here did not include measurements of the upwind temperature and wind profiles with the temporal and spatial resolution needed to determine the cause of the sudden flow transitions or to evaluate the suitability of hydraulic-flow analogs. In the future, we plan to perform numerical simulations of Meteor Crater with high-resolution models to gain a better understanding of the different flow regimes and the responsible mechanisms. The crater provides an opportunity to compare model results with observations for an almost-idealized enclosed basin and, thus, to verify model performance.

Acknowledgments. This material is based upon work supported by the National Science Foundation (NSF) under Grants ATM-0444205 and -0837870. Any opinions, findings, and conclusions or recommendations expressed in this material are those of the authors and do not necessarily reflect the views of the NSF. Author BA was supported by a *Stipendium* from the Karlsruhe House of Young Scientists (KHYS) and a *Kurzstipendium für Doktoranden* from the Deutscher Akademischer Austauschsdienst (DAAD). SWH received support from Army Research Office Grant 52734-EV. Author ML was supported by a DOC-fFORTE fellowship from the Austrian Academy of Sciences. We thank the Barringer Crater Company and Meteor Crater Enterprises, Inc., for access to the field site and Maura Hahnenberger for processing the tethersonde data. The National Center for Atmospheric Research's Earth Observing Laboratory provided equipment, field support, and quality-controlled datasets. The staffs of the NCAR Integrated Sounding System and Integrated Surface Flux Facility are thanked for their field and data-processing assistance. We thank Dale Durran for useful comments on this manuscript.

REFERENCES

Baines, P. G., 1995: *Topographic Effects in Stratified Flows*. Cambridge University Press, 482 pp.

Clements, C. B., C. D. Whiteman, and J. D. Horel, 2003: Cold-air-pool structure and evolution in a mountain basin: Peter Sinks, Utah. *J. Appl. Meteor.,* **42,** 752–768.

Durran, D. R., 1986: Another look at downslope windstorms. Part I: The development of analogs to supercritical flow in an infinitely deep, continuously stratified fluid. *J. Atmos. Sci.,* **43,** 2527–2543.

——, 2003: Downslope winds. *Encyclopedia of Atmospheric Sciences,* J. Holton, J. A. Curry, and J. A Pyle, Eds., Elsevier, 644–650.

Fritts, D. C., D. Goldstein, and T. Lund, 2010: High-resolution numerical studies of stable boundary layer flows in a closed basin: Evolution of steady and oscillatory flows in an axisymmetric Arizona Meteor Crater. *J. Geophys. Res.,* **115,** D18109, doi:10.1029/2009JD013359.

Haiden, T., C. D. Whiteman, S. W. Hoch, and M. Lehner, 2011: A mass flux model of nocturnal cold-air intrusions into a closed basin. *J. Appl. Meteor. Climatol.,* **50,** 933–943.

Hoch, S. W., C. D. Whiteman, M. Lehner, D. Martínez, and M. Kossmann, 2010: Interaction of regional scale drainage flows with the nocturnal stable atmosphere in Arizona's Meteor Crater. Preprints, *14th Conf. on Mountain Meteorology,* Lake Tahoe, CA, Amer. Meteor. Soc., P2.12. [Available online at http://ams.confex.com/ams/pdfpapers/173739.pdf.]

Jiang, Q., and R. B. Smith, 2003: Gravity wave breaking in two-layer hydrostatic flow. *J. Atmos. Sci.,* **60,** 1159–1172.

Kring, D. A., 2007: Guidebook to the geology of Barringer Meteorite Crater, Arizona (a.k.a Meteor Crater). Lunar and Planetary Institute Contribution 1355, 150 pp. [Available online at http://www.lpi.usra.edu/publications/books/barringer_crater_guidebook/.]

Lilly, D. K., 1978: A severe downslope windstorm and aircraft turbulence event induced by a mountain wave. *J. Atmos. Sci.,* **35,** 59–77.

Long, R. R., 1954: Some aspects of the flow of stratified fluids II: Experiments with a two-fluid system. *Tellus,* **6,** 97–115.

Mayr, G. J., and L. Armi, 2008: Föhn as a response to changing upstream and downstream air masses. *Quart. J. Roy. Meteor. Soc.,* **134,** 1357–1369.

——, and ——, 2010: The influence of downstream diurnal heating on the descent of flow across the sierras. *J. Appl. Meteor. Climatol.,* **49,** 1906–1912.

Nappo, C., 2002: *An Introduction to Atmospheric Gravity Waves*. Academic Press, 276 pp.

Peltier, W. R., and T. L. Clark, 1979: The evolution and stability of finite-amplitude mountain waves. Part II: Surface wave drag and severe downslope windstorms. *J. Atmos. Sci.,* **36,** 1498–1529.

Savage, L., I. Crosby, S. Zhong, W. Yao, W. J. O. Brown, T. W. Horst, and C. D. Whiteman, 2008: An observational and numerical study of a regional-scale downslope flow in northern Arizona. *J. Geophys. Res.,* **113,** D14114, doi:10.1029/2007JD009623.

Smith, R. B., 1985: On severe downslope winds. *J. Atmos. Sci.,* **42,** 2597–2603.

——, 2003: Stratified flow over topography. *Environmental Stratified Flows,* P. Chatwin et al., Eds., Springer, 119–159.

——, and J. Sun, 1987: Generalized hydraulic solutions pertaining to severe downslope winds. *J. Atmos. Sci.,* **44,** 2934–2939.

Steinacker, R., and Coauthors, 2007: A sinkhole field experiment in the eastern Alps. *Bull. Amer. Meteor. Soc.,* **88,** 701–716.

Viana, S., C. Yagüe, G. Maqueda, and G. Morales, 2007: Study of the surface pressure fluctuations generated by waves

and turbulence in the nocturnal boundary layer during SABLES2006 field campaign. *Fís. Tierra,* **19,** 55–71.

Whiteman, C. D., 2000: *Mountain Meteorology: Fundamentals and Applications*. Oxford University Press, 355 pp.

——, T. B. McKee, and J. C. Doran, 1996: Boundary layer evolution within a canyonland basin. Part I: Mass, heat, and moisture budgets from observations. *J. Appl. Meteor.,* **35,** 2145–2161.

——, and Coauthors, 2008: METCRAX 2006: Meteorological experiments in Arizona's Meteor Crater. *Bull. Amer. Meteor. Soc.,* **89,** 1665–1680.

——, S. W. Hoch, M. Lehner, and T. Haiden, 2010: Nocturnal cold-air intrusions into a closed basin: Observational evidence and conceptual model. *J. Appl. Meteor. Climatol.,* **49,** 1894–1905.

Wilczak, J., S. Oncley, and S. Stage, 2001: Sonic anemometer tilt correction algorithms. *Bound.-Layer Meteor.,* **99,** 127–150.